Fast Laplace solver approach to pore-scale permeability

C. H. Arns
School of Petroleum Engineering, University of New South Wales, Sydney, NSW 2052, Australia

P. M. Adler
UPMC Sisyphe, Boîte 105, 4 place Jussieu, 75252 Paris cedex 05, France

(Received 8 June 2017; revised manuscript received 5 September 2017; published 14 February 2018)

We introduce a powerful and easily implemented method to calculate the permeability of porous media at the pore scale using an approximation based on the Poiseulle equation to calculate permeability to fluid flow with a Laplace solver. The method consists of calculating the Euclidean distance map of the fluid phase to assign local conductivities and lends itself naturally to the treatment of multiscale problems. We compare with analytical solutions as well as experimental measurements and lattice Boltzmann calculations of permeability for Fontainebleau sandstone. The solver is significantly more stable than the lattice Boltzmann approach, uses less memory, and is significantly faster. Permeabilities are in excellent agreement over a wide range of porosities.

DOI: 10.1103/PhysRevE.97.023303

I. INTRODUCTION

Calculating the permeability of a porous medium following the Stokes equation for laminar flow is a frequent problem in various applications from geophysics to material science [1,2]. However, the direct calculation of permeability from discrete presentations of microstructure as, e.g., acquired through x-ray-CT imaging is a computationally challenging task. The calculations are often carried out using finite volume (on structured or unstructured meshes), finite difference, or lattice Boltzmann techniques under high computational cost. Furthermore, for the stable solution of the Stokes equation with lattice Boltzmann techniques a critical radius of 4–5 voxels is required to avoid negative permeabilities [3], which may incur additional computational costs due to resampling requirements or prevent numerical solution of the problem requiring a large field of view, e.g., due to structural heterogeneity. Methods to reduce the computational cost include abstractions of the underlying pore space into simply connected elements constituting network models. In those models, the conductance of the individual connections between nodes are estimated using, e.g., a hydraulic radius approximation [4]. The level of abstraction required by these techniques often leads to reduced accuracy in the prediction of transport properties, in particular if the shape of the pores is complex and/or the actual definition of pores is difficult. It would be desirable to have a method which uses the complex structure provided by image-based three-dimensional (3D) representations of the microstructure that preserves the geometrical details, while allowing significantly faster and/or more numerically stable solutions. One method in use for more than a decade in the digital core analysis area is based on the excellent correlation of permeability with formation factor and critical radius, utilizing the Katz-Thompson correlation [3,5,6]. This method requires the solution of a Laplace equation and Stokes equation for the establishment of a correlation coefficient, followed by an up-scaling step where the same correlation coefficient is applied regardless of the scale change.

This paper presents a Laplace approximation for the solution of the Stokes equation on the basis of an extension of Poiseuille's law to complex microstructures using Euclidean distance maps to approximate local voxelwise conductances. Contrary to an approximation given in Ref. [7], which involves distances with reference to the center of a flow path (medial axis), we directly use the Euclidean distance map and show that due to discretization effects the approximation is accurate despite being based on surface distances, which makes the approximation easy to implement.

The paper is organized as follows. Section II recalls the Stokes equation and details the Laplace approximation. For parallel flows, the solution of the Laplace equation is given by the classical parallel formula [1]. This solution is applied to elementary configurations such as circular pipes and rectangular channels. The numerical codes used to solve the Stokes and Laplace equations are briefly described. Section III compares the Laplace approximation to some existing analytical solutions such as circular pipes and rectangular channels, but also two-dimensional (2D) and 3D sinusoidal channels and simple cubic arrays of spheres. In Sec. IV the Laplace approximation is applied to a real fracture and to real Fontainebleau sandstones. The results are compared with the numerical calculations obtained with the lattice Boltzmann method. Finally, concluding remarks are made in Sec. V.

II. GENERAL

A. The Stokes equations

The low Reynolds number flow of an incompressible Newtonian fluid is governed by the usual Stokes equations

$$\nabla p = \mu_f \nabla^2 \boldsymbol{v}, \quad \nabla \cdot \boldsymbol{v} = 0, \tag{1a}$$

where $\boldsymbol{v}$, p, and μ_f are the local velocity, local pressure, and viscosity of the fluid, respectively. In general, $\boldsymbol{v}$ satisfies the no-slip condition at the wall S_p:

$$\boldsymbol{v} = 0 \ \text{ on } S_p. \tag{1b}$$

Moreover, the fluid moves under the action of a macroscopic pressure gradient $\overline{\nabla p}$.

Analytical solutions of this problem are known for a range of structures, and we will use these to test the numerical method in Sec. III. Most solutions are obtained numerically.

When a solution $\boldsymbol{v}$ is derived, the seepage velocity $\overline{\boldsymbol{v}}$ is obtained by averaging over the pore volume V_p contained in the volume V. Because of the linearity of the Stokes equations, $\overline{\boldsymbol{v}}$ is proportional to the macroscopic pressure gradient,

$$\overline{\boldsymbol{v}}_S = \frac{1}{V}\int_{V_p} \boldsymbol{v}\, d^3r = -\frac{1}{\mu_f}\boldsymbol{K}\cdot\overline{\nabla p}, \tag{2}$$

where the tensor $\boldsymbol{K}$ denotes the permeability.

B. The Laplace approximation

The main objective of this paper is to propose and to assess an approximate solution to the Stokes equation based on the following assumption. The space is divided into elementary cubes (or voxels) of size a which are either filled with fluid or solid. The Euclidean distance $r(x,y,z)$ of each pore voxel to the solid interface is calculated. Each voxel in the pore space is assigned the smallest center to center distance on the lattice to the closest voxel not member of the pore space. The distance is calculated using an message passing interface (MPI) parallel implementation of algorithm four of Ref. [8]. This algorithm calculates the exact Euclidean distance map by executing successive forward and backward scans of the structure in the x, y, and z directions and has excellent scaling behavior.

For laminar flow through infinite cylindrical pipes with no-slip boundary condition on the wall the axially symmetric velocity profile is described by Hagen-Poiseuille's law [9]:

$$u(r) = -\frac{1}{4\mu_f}\frac{dP}{dx}(R^2 - r^2). \tag{3}$$

Comparison of this exact relation with the Darcy law (2) suggests giving each voxel a permeability $k(x,y,z)$ expressed by (3)

$$k(x,y,z) = [r(x,y,z) - \alpha a]^2, \tag{4a}$$

where α is an arbitrary constant ranging from 0 to 1. Most likely, α is taken equal to 0.5 since it corresponds to the voxel centers. In this formula, $r(x,y,z)$ denotes the distance between the center of the voxel to the closest wall augmented by $0.5\,a$. The local seepage velocity $\boldsymbol{v}_L(x,y,z)$ can be expressed as

$$\boldsymbol{v}_L(x,y,z) = -\frac{k}{\mu_f}\nabla p. \tag{4b}$$

The approximate macroscopic permeability $\boldsymbol{K}_L$ of the porous medium can be obtained by solving the elliptical equation

$$\nabla\cdot(k\nabla p) = 0. \tag{5a}$$

Since the solid phase is impervious, the boundary condition at the solid interface with unit normal $\boldsymbol{n}$ is

$$\boldsymbol{n}\cdot\nabla p = 0. \tag{5b}$$

Again a macroscopic pressure gradient $\overline{\nabla p}$ is applied on the unit cell along the three axes successively, and the corresponding pressure fields are calculated. The approximate seepage velocity $\overline{\boldsymbol{v}}_L$ is obtained by averaging the local seepage velocity $\boldsymbol{v}_L(x,y,z)$ over the unit cell. The approximate permeability tensor $\boldsymbol{K}_L$ is derived from a Darcy equation similar to (2)

$$\overline{\boldsymbol{v}}_L = -\frac{1}{\mu_f}\boldsymbol{K}_L\cdot\overline{\nabla p}. \tag{6}$$

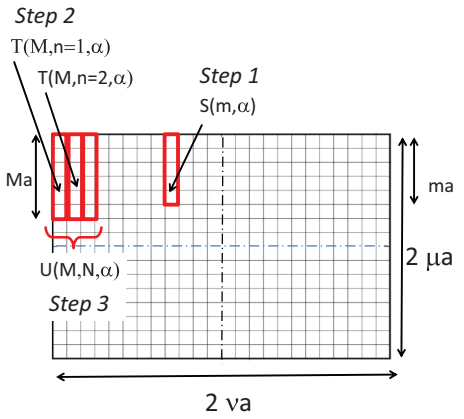

FIG. 1. Analytical solution of the Laplace equation for parallel flows and illustration of the three steps. Step 1: $S(m,\alpha)$ is drawn for $m = 5$. Step 2: $T(M,n,\alpha)$ is illustrated three times for $M = 6$ and $n = 1, 2, 3$. Step 3: $U(M,N,\alpha)$ is illustrated for $M = 6$ and $N = 3$.

C. Analytical solutions of the Laplace approximation for parallel flows

In several elementary configurations for which analytical solutions of the Stokes equation exist, flow occurs along parallel streamlines. As a general rule, when two independent porous blocks are located one beside the other with the same area perpendicular to the overall pressure drop, the effective permeability is equal to the arithmetic average. This is easily extended to N blocks of permeabilities K_n $(n = 1,2,\ldots,N)$ located one beside the other:

$$K = \frac{1}{N}\sum_{n=1}^{N} K_n. \tag{7}$$

The evaluation of this sum necessitates several steps which are illustrated in Fig. 1 for a rectangular channel of size $(2\nu a, 2\mu a)$ with $\nu \geqslant \mu$. The sum should be evaluated over all the voxels which pave the channel.

First, consider a strip of length m perpendicular to a wall, starting from a wall, but without any interaction with another wall. The sum $S(m,\alpha)$ of the individual permeabilities is (cf. step 1 in Fig. 1)

$$S(m,\alpha) = \sum_{k=1}^{m}(k-\alpha)^2. \tag{8}$$

In order to evaluate this sum and some others, it is useful to recall the following relations [10]:

$$\sum_{k=1}^{m} k = \frac{m(m+1)}{2}, \quad \sum_{k=1}^{m} k^2 = \frac{m(m+1)(2m+1)}{6},$$
$$\sum_{k=1}^{m} k^3 = \left[\frac{m(m+1)}{2}\right]^2. \tag{9}$$

Straightforward calculations yield

$$S(m,\alpha) = m\alpha^2 - m(m+1)\alpha + \frac{m(m+1)(2m+1)}{6}. \quad (10)$$

Consider now strips of length M close to a solid wall and denote by n the distance of the line to the wall (cf. step 2 in Fig. 1). When the line actually touches the wall, its distance is equal to 1, and the sum of the local permeabilities is simply

$$T(M,n=1,\alpha) = M(1-\alpha)^2. \quad (11a)$$

The sums for the next lines at distances $n = 2$ and 3 are equal to

$$\begin{aligned} T(M,n=2,\alpha) &= (1-\alpha)^2 + (M-1)(2-\alpha)^2, \\ T(M,n=3,\alpha) &= (1-\alpha)^2 + (2-\alpha)^2 + (M-2)(3-\alpha)^2. \end{aligned} \quad (11b)$$

More generally, for $n \geqslant 2$,

$$T(M,n,\alpha) = \sum_{k=1}^{k=n-1} (k-\alpha)^2 + (M+1-n)(n-\alpha)^2. \quad (11c)$$

This sum can be evaluated by using (10) again:

$$\begin{aligned} T(M,n,\alpha) = {} & M\alpha^2 + n\left(\tfrac{1}{6} - \alpha - 2\alpha M\right) \\ & + n^2\left(M + \alpha + \tfrac{1}{2}\right) - \tfrac{2}{3}n^3 \quad \text{for } n \geqslant 2. \end{aligned} \quad (12)$$

The last evaluation that is needed is the sum $U(M,N,\alpha)$ of N lines of length M close to a wall (cf. step 3 in Fig. 1):

$$U(M,N,\alpha) = T_1 + \sum_{n=2}^{N} T(M,n,\alpha). \quad (13a)$$

Introduction of (12) into (13a) and use of (10) yields

$$\begin{aligned} U(M,N,\alpha) = {} & M(1-\alpha)^2 - \frac{2}{3}\left\{\left[\frac{N(N+1)}{2}\right]^2 - 1\right\} \\ & + \left(M + \alpha + \frac{1}{2}\right)\left[\frac{N(N+1)(2N+1)}{6} - 1\right] \\ & + \left(\frac{1}{6} - \alpha - 2\alpha M\right)\left[\frac{N(N+1)}{2} - 1\right] \\ & + M(N-1)\alpha^2. \end{aligned} \quad (13b)$$

Then useless complications are avoided by considering squares and rectangles with an even number of voxels along each direction, i.e., squares of side $\ell = 2\mu a$ and rectangles of sides $\ell = 2\mu a, L = 2\nu a$ where μ and ν verify $\nu \geqslant \mu \geqslant 2$. Since the sum should cover the whole channel, the Laplace approximations K_{Lsq} and K_{Lrec} can be expressed as

$$\begin{aligned} K_{Lsq} &= a^2 \frac{U(\mu,\mu,\alpha)}{\mu^2}, \\ K_{Lrec} &= a^2 \frac{U(\mu,\mu,\alpha) + (\nu-\mu)S(\mu,\alpha)}{\mu\nu}. \end{aligned} \quad (14a)$$

These quantities are made dimensionless by the square of the smaller side $2\mu a$:

$$\begin{aligned} K'_{Lsq} &= \frac{U(\mu,\mu,\alpha)}{4\mu^4}, \\ K'_{Lrec} &= \frac{U(\mu,\mu,\alpha) + (\nu-\mu)S(\mu,\alpha)}{4\mu^3\nu}. \end{aligned} \quad (14b)$$

Let r be the aspect ratio of the rectangular channel:

$$r = \frac{L}{\ell} = \frac{\nu}{\mu}. \quad (15)$$

It is interesting to derive the continuous limit of the expressions (14) when μ and ν tend towards infinity. For rectangles, μ and ν keep a constant aspect ratio r:

$$K'_{Lsq,\infty} = \frac{1}{24}, \quad K'_{Lrec,\infty} = \frac{2r-1}{24r}. \quad (16)$$

D. Numerical solutions

1. Lattice Boltzmann approach

For complex geometries such as fractures and 3D real porous media, there is no analytical solution to the Stokes equations which can be numerically solved by a variety of methods such as the lattice Boltzmann method (LBM). Originally devised as a generalization of lattice gas automata [11], it can be also derived by an adequate discretization of the continuous Boltzmann equation [12]. In this work we utilize the D3Q19 model for three space dimensions with 19 microscopic velocities [13]; for a better precision, the model is TRT, i.e., with two relaxation times [14,15], for the comparisons to the analytical models. We use a fluid viscosity of $\nu = \frac{1}{6}$ corresponding to a single relaxation time of $\tau = 1$ or $s_2 = 1/\tau$ and $s_2 = 8\frac{2\tau-1}{8\tau-1}$ for the even and odd order relaxation rates of the TRT approach. Periodic boundary domain conditions are applied and the midway bounce back rule on the fluid-solid boundary. The implementation of the solver is similar to that of Ref. [16]. The pressure gradient on the fluid is realized by application of a body force [17]. For the application to real porous media we utilize an MPI parallel version of the single relaxation time (SRT) solver used in Refs. [3,18]. The MPI implementation uses a Cartesian decomposition technique and assigns storage only to fluid and fluid-solid boundary nodes while at the same time minimizing message sizes between processors. A 15-voxel-thick free fluid layer [19] is applied to realize the periodic boundary conditions.

2. The Laplace equation

First, the Euclidean distance map should be determined by using the algorithm summarized in Sec. II B; the computational time necessary for this step is negligible. Then the permeability field is derived.

Second, the solution of the Laplace equation is obtained by the following numerical techniques. The medium is discretized in elementary cubes of a given permeability. The unknown pressures are located at the corners of these cubes. The Laplace equation is discretized by the so-called box integration method [20]. Spatially periodic boundary conditions are applied along the three directions of space. The resulting linear system is solved by a classical conjugate gradient algorithm. An

application to a real set of permeability field is provided by Ref. [21].

III. COMPARISON WITH EXACT SOLUTIONS

A. Elementary shapes

The permeabilities of a circular pipe, a square, and a plane channel have been known for a long time, and their derivation can be found in Ref. [9]. The simplest ones are for a plane channel of width ℓ and a circular channel of radius R:

$$K'_{\text{plane}} = \frac{K_{\text{plane}}}{\ell^2} = \frac{1}{12}, \quad K'_{cir} = \frac{K_{cir}}{R^2} = \frac{1}{8}. \tag{17}$$

The analytical solution for square and rectangular channels with sides L and ℓ is again given by Ref. [9]. Let ℓ be the smaller side of the channel. The permeability K is made dimensionless by ℓ^2. Therefore,

$$K'_S = \frac{K_S}{\ell^2} = \frac{1+r^2}{24} - \frac{8}{\pi^5}\mathcal{S}, \tag{18a}$$

where

$$\mathcal{S} = \sum_{n=1}^{\infty} \frac{1}{(2n+1)^5} \times \left[r^3 \tanh\left(\frac{2n-1}{2}\frac{\pi}{r}\right) + \frac{1}{r}\tanh\left(\frac{2n-1}{2}\pi r\right)\right] \tag{18b}$$

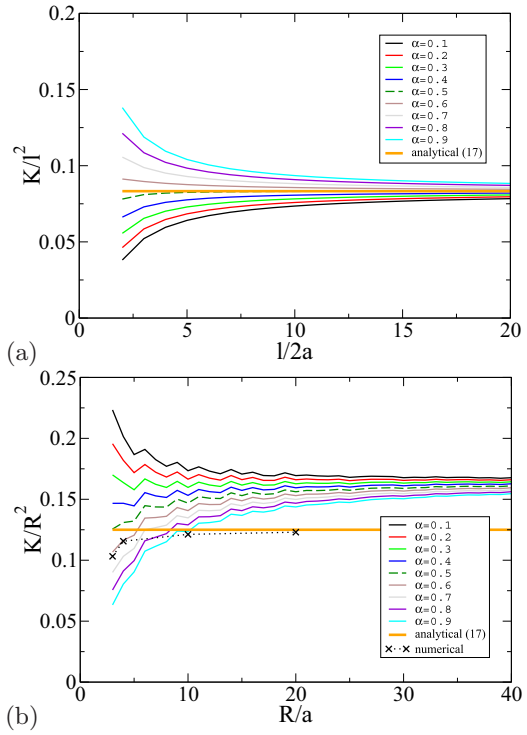

FIG. 2. Comparison between the analytical solution (17) (thick solid lines) and the analytical solution (14) for the Laplace equation for various values of the parameter α (thin solid lines). Data are for $\alpha = 0.1, 0.2, ..., 0.9$. The broken lines correspond to $\alpha = 0.5$. (a) Plane channel, (b) circular channel; the dotted line corresponds to the numerical solution by a classical code.

and r is the aspect ratio (15). The permeability of a square channel can be derived as a direct consequence:

$$K'_{S,sq} = 0.035144\ldots. \tag{18c}$$

In these cases, the flow occurs along parallel streamlines, and the analytical solutions proposed in Sec. II C can be used for a direct comparison, except for the circular pipe where the pore space cannot be described simply.

This relation is displayed in Fig. 2 for the two simplest configurations which are the circular and the plane channels. The influence of the discretization of the channel and of α is studied. A first general remark can be made; the permeability is a decreasing function of α. There is a strong contrast between these two cases.

The agreement for a plane channel is almost perfect whatever the width of the channel for $\alpha = 0.5$. For large values of the discretization, it tends towards the exact limit $1/12$ as indicated by (16).

The comparison is less good for circular pipes. It is interesting to note that the comparison is relatively better for a poor discretization. This is expected since for low resolution the cross section of a pipe is not circular (in voxels). In that case the theoretical formula is not working so well (since it is not strictly circular) and at the same time LBM struggles at low resolution more than a Laplace solver. The influence of α is large for small values of the radius. For large values of the radius, the results tend towards $1/6$ as it can be shown by considering the integral:

$$K_{Lcir,\infty} = \frac{1}{\pi R^4}\int_0^R 2\pi\rho\, d(R-\rho)^2 = \frac{1}{6}. \tag{19}$$

A slightly more complex configuration is the rectangular channel which has been studied by different means. The Laplace approximation is compared to the Stokes equation in Figs. 3 and 4. The first set of figures shows the influence of the aspect ratio, the parameter α, and the discretization; the data are compared to the analytical solution (18). The dimensionless permeability is seen to be again a decreasing function of α; it is an increasing function of the aspect ratio as it should. Finally, the discretization ℓ/a has a strong influence on the data; all the curves gather around the theoretical values when ℓ/a increases.

The second figure compares the permeability for an infinite discretization as a function of the aspect ratio. As indicated by (16), α does not play any role in this limit. The agreement between the exact analytical solution (18) and the Laplace approximation (16) is excellent; there is only a slight discrepancy for square channels where these two solutions correspond to 0.0351 and 0.0417, respectively. This agreement and (16) suggest a simple interpolation:

$$K'_{Lsq,\infty} = \frac{2r - 2 + 24\times 0.0351}{24r} = \frac{2r - 1.1576}{24r}. \tag{20}$$

This elementary interpolation is seen to be very good in Fig. 4.

A check of the numerical solution of the Laplace equation was made for flows in square and rectangular channels. These solutions were found in perfect agreement with the predictions of the parallel formulas (14); it was not found useful to report them here.

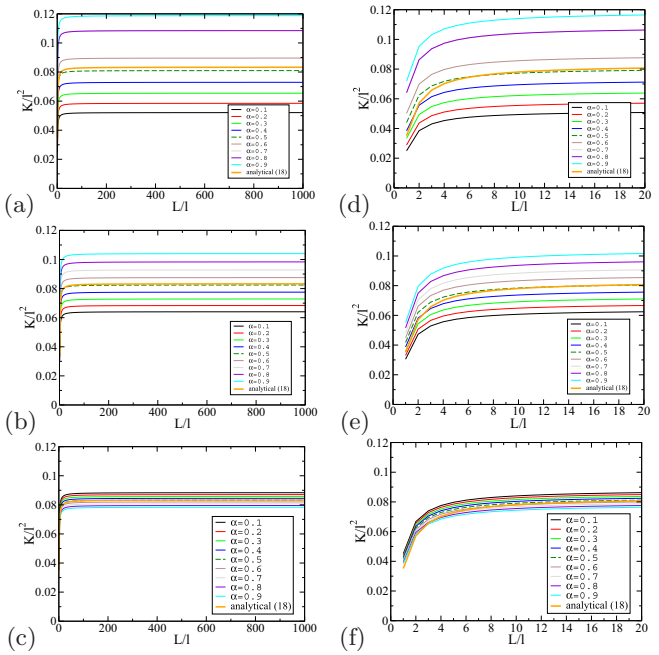

FIG. 3. Rectangular channels. Comparison between the analytical solution (18) (thick solid line) and the analytical solution (14) for the Laplace equation for various values of the parameter α (thin solid lines). Data are for $\alpha = 0.1$, 0.2, ..., 0.9. The thick broken lines correspond to $\alpha = 0.5$. The various subfigures are for various discretizations: $\ell/a = 6$ (a, d), 10 (b, e), 40 (c, f); the right column depicts small L behavior.

As a conclusion of this first set of comparisons, it can be said that the value 0.5 for the parameter α is the most logical and the one which provides the best comparison with the theoretical predictions at least for rectangular channels. Therefore, the calculations are limited to the case $\alpha = 0.5$ in the rest of this paper.

B. Sinusoidal channels

1. 2D sinusoidal channels

Formal expansions for the permeability of channels with wavy walls were devised in Ref. [22]. Detailed results are given for the following channel:

$$z = b(1 + \eta \cos x), \quad z = b(1 - \epsilon \cos x). \tag{21}$$

The permeability is compared to the permeability for a channel with parallel walls and of width $2b$ which is equal to $b^2/3$. Note

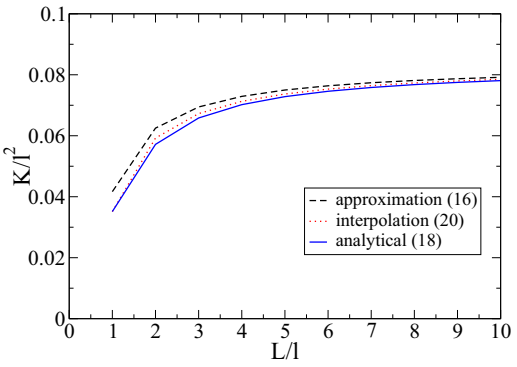

FIG. 4. The dimensionless permeability $K' = K/\ell^2$ for square and rectangular channels as a function of the aspect ratio $r = L/\ell$. Data are for analytical solution (18) (solid line), Laplace approximation (16) (broken line), interpolation between the square and the plane channel (20) (dotted line).

that b is dimensionless in this subsection. The corresponding dimensionless value $K'_{xx,an}$ along the x axis for $b = 0.5$ is given by the expansion [their relation (58)]

$$\begin{aligned} K'_{xx,an} = {} & 1. - 3.14963\eta^2 + 4.08109\eta^4 - 3.48479\eta^6 \\ & + 2.93797\eta^8 - 2.56771\eta^{10} + 2.21983\eta^{12} \\ & - 1.93018\eta^{14} + 1.67294\eta^{16} - 1.45302\eta^{18} \\ & + 1.26017\eta^{20} - 1.09411\eta^{22} + 0.949113\eta^{24} \\ & - 0.823912\eta^{26} + 0.714804\eta^{28} 0.620463\eta^{30} \\ & + O(\eta^{32}). \end{aligned}$$

The calculations were performed in the following way. First, the number of voxels along the z axis is chosen. The channel lies in the first $N_{cz} - 1$ voxels since the last horizontal layer remains solid to ensure no flow along this direction. Therefore, the size a of the voxel is

$$a = \frac{2b(1 + \eta)}{N_{cz} - 1}. \tag{22a}$$

Since the length of one period is 2π, the number of voxels along the x axis is

$$N_{cx} = \frac{2\pi}{a}. \tag{22b}$$

TABLE I. Symmetric sinusoidal 2D channel. The diagonal components K'_{Lxx}, K'_{Lyy} of the permeability tensor calculated by the Laplace equation, the y component K'_{par} calculated by the parallel formula, the analytical expansion $K'_{xx,an}$ (22) of Ref. [22], and the diagonal components $K'_{xx,\text{LBM}}$, $K'_{yy,\text{LBM}}$ calculated by a lattice Boltzmann algorithm; $\alpha = 0.5$.

Dimensions	K'_{Lxx}	K'_{Lyy}	K'_{par}	$K'_{xx,an}$	$K'_{xx,\text{LBM}}$	$K'_{yy,\text{LBM}}$
$\eta = 0.2$, $26 \times 3 \times 6$	0.6132	0.9396	0.9396	0.880	0.468	0.7326
$\eta = 0.2$, $52 \times 3 \times 11$	0.6144	0.8413	0.8413	0.880	0.596	0.7958
$\eta = 0.2$, $105 \times 3 \times 21$	0.7308	0.87	0.87	0.880	0.718	0.8509
$\eta = 0.2$, $262 \times 3 \times 51$	0.7224	0.8636	0.8636	0.880	0.728	0.8659
$\eta = 0.4$, $22 \times 3 \times 6$	0.7159	1.0538	1.0538	0.4226	0.5434	0.8121
$\eta = 0.4$, $45 \times 3 \times 11$	0.3078	0.8100	0.8100	0.4226	0.3149	0.7673

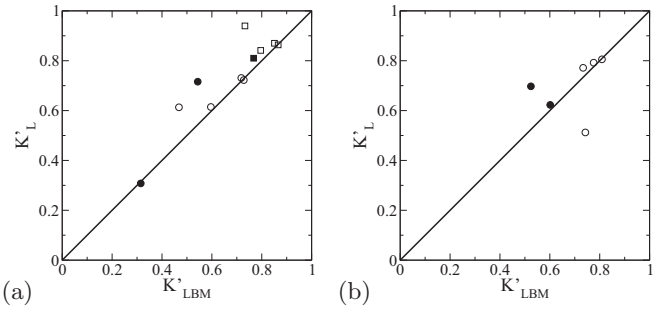

FIG. 5. Comparison between the Laplace and the lattice Boltzmann dimensionless permeabilities for 2D and 3D sinusoidal channels. $\alpha = 0.5$. (a) 2D channels; data are for K'_{xx} (○), K'_{yy} (□); $\eta = 0.2$ (filled dots), 0.4 (filled squares). (b) 3D channels; data are for $\eta = 0.2$ (empty dots), 0.4 (filled dots).

The average width $2b$ of the channel in lattice units is

$$\frac{2b}{a} = \frac{N_{cz} - 1}{1 + \eta}. \tag{22c}$$

The channel is assumed to be infinite along the y axis. Spatially periodic boundary conditions are applied along this axis, and a value of 3 was chosen for $N_{cy} - 1$.

The various results are gathered in Table I, which is illustrated by Fig. 5(a).

When the discretization of the sinusoidal wall is poor, the numerically solved geometry is very different from the theoretical one. Therefore, any numerical estimation of the permeability is expected to be far from the analytical predictions. Because of this unavoidable discrepancy between the numerical estimation $K'_{xx,\mathrm{LBM}}$ and the analytical prediction $K'_{xx,an}$ for poor discretizations, it is better to compare the Laplace approximation K'_{Lxx} to $K'_{xx,\mathrm{LBM}}$. This comparison becomes better for fine discretizations, whatever the value of η. The quality of the comparison does not depend on the component of the permeability tensor.

2. 3D sinusoidal channels

Detailed results are given for the following channel by [22]

$$z = \pm b\left[1 + \tfrac{1}{2}\eta\{\cos(x + y) + \cos(x - y)\}\right]. \tag{23}$$

The permeability is again compared to the permeability of a channel with parallel walls and of width $2b$, which is equal to $b^2/3$. The corresponding dimensionless value $K'_{xx,an}$ along the x axis for $b = 0.3$ is given by the expansion [their relation (68)]

$$\begin{aligned} K'_{xx,an} = {} & 1. - 0.465674\eta^2 + 0.329218\eta^4 - 0.261666\eta^6 \\ & + 0.004467\eta^8 - 0.0386987\eta^{10} - 0.0177808\eta^{12} \\ & - 0.0239319\eta^{14} + O(\eta^{16}). \end{aligned}$$

Again the number of voxels along the z axis is chosen first. Then the relations (22) are still valid, and they are applied for $b = 0.3$. Now N_{cx} and N_{cy} are equal. The permeability components along the x and y axes are also equal.

The various results are gathered in Table II, which is illustrated by Fig. 5(b). Qualitatively, the conclusions are the same as for the 2D channel.

TABLE II. Symmetric sinusoidal 3D channel. The diagonal component K'_{Lxx} of the permeability tensor calculated by the Laplace equation, the analytical expansion $K'_{xx,an}$ (24) of Ref. [22], and the diagonal component $K'_{xx,\mathrm{LBM}}$ calculated by a lattice Boltzmann algorithm; $\alpha = 0.5$.

Dimensions	K'_{Lxx}	$K'_{xx,an}$	$K'_{xx,\mathrm{LBM}}$
$\eta = 0.2$, $44 \times 44 \times 6$	0.5123	0.9819	0.7424
$\eta = 0.2$, $87 \times 87 \times 11$	0.7715	0.9819	0.7335
$\eta = 0.2$, $175 \times 175 \times 21$	0.7920	0.9819	0.7757
$\eta = 0.2$, $436 \times 436 \times 51$	0.8056	0.9819	0.8089
$\eta = 0.4$, $37 \times 37 \times 6$	0.6973	0.9328	0.5241
$\eta = 0.4$, $75 \times 75 \times 11$	0.6228	0.9328	0.6014

C. Simple cubic arrays of spheres

Another geometry which can be analytically addressed is the cubic packings of spheres [23,24] which are spatially periodic. These packings are also of historical importance since they were for a long time considered as model porous media; moreover, they represented nonconsolidated media such as sands and particle packings. The results were represented in terms of the dimensionless drag coefficient k_{ZH}, which can be related to the theoretical permeability K_{th} by

$$K_{th} = \frac{2R^2}{9ck_{\mathrm{ZH}}}, \tag{24}$$

where R is the sphere radius and c the solid concentration.

Such configurations can be studied by four different means, namely, by an application of the Laplace equation in which case K_L is derived or by resolution of the Stokes equation (1). This latter resolution can be obtained theoretically according to (24); it can also be numerically derived by LBM as summarized in Sec. II D 1, and by a classical method [25] which uses an artificial compressibility with a staggered marker-and-cell (MAC) mesh and which yields a permeability denoted by K_{MAC}.

Two values of c were numerically addressed. A solid particle of radius $R/a = 18$ is located in a cubic unit cell of size $49a$. The corresponding solid concentration c when the sphere is discretized in elementary voxels of size a is 0.207. In Table 2 of Ref. [23], k_{ZH} is given and equal to 7.44. Therefore, the resulting permeability K_{th} according to (24) can be readily

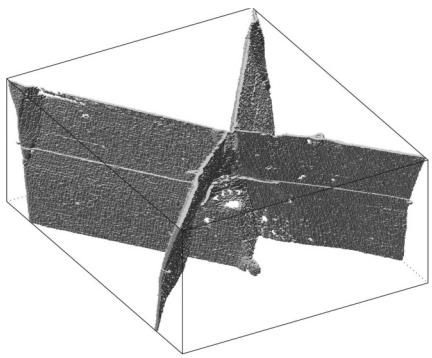

FIG. 6. Subsample of a tight sandstone measured by Focussed Ion Beam/Scanning Electron Microscope (FIB/SEM). It was displayed in Fig. 8(a) of Ref. [26] under the name sech1.

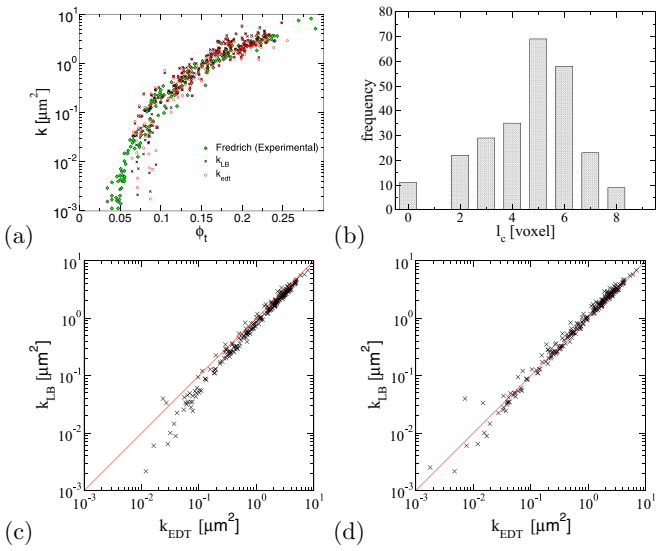

FIG. 7. Comparison of numerically derived and experimentally measured permeability for Fontainebleau sandstone. The accuracy of the numerical calculations (in particular k_{LB}) breaks down at permeabilities below $k \approx a^2$, where $a = 5.68\,\mu$m is the resolution of the image. (a) k_{EDT} and k_{LB} as function of porosity against experiment, $a = 5.68\,\mu$m; (b) distribution of critical diameters for $a = 5.68\,\mu$m; (c) k_{EDT} vs k_{LB} at $a = 5.68\,\mu$m; (d) k_{EDT} vs k_{LB} at $a = 2.84\,\mu$m.

compared to the values obtained by other means:

$$\frac{K_{th}}{a^2} = 46.6, \quad \frac{K_L}{a^2} = 43.3,$$
$$\frac{K_{LBM}}{a^2} = 48.1, \quad \frac{K_{\mathrm{MAC}}}{a^2} = 46.3. \tag{25}$$

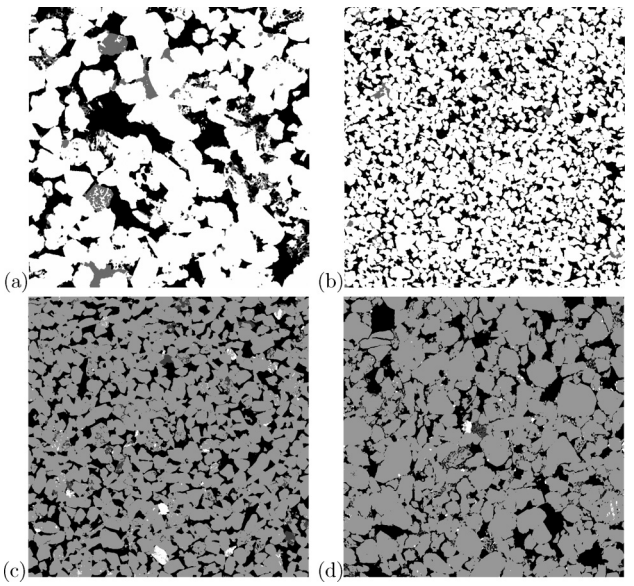

FIG. 8. Cross sections through cubic subdomains of segmented tomograms of four outcrop sandstone samples: (a) Berea sandstone (750^3 voxels, $a = 2.33\,\mu$m); (b) Bentheimer sandstone (1200^3 voxels, $a = 5.39\,\mu$m); (c) Castlegate sandstone (900^3 voxels, $a = 3.36\,\mu$m); (d) Leopard sandstone (900^3 voxels, $a = 2.15\,\mu$m). White and light gray indicate denser phases (resolved pore space is black).

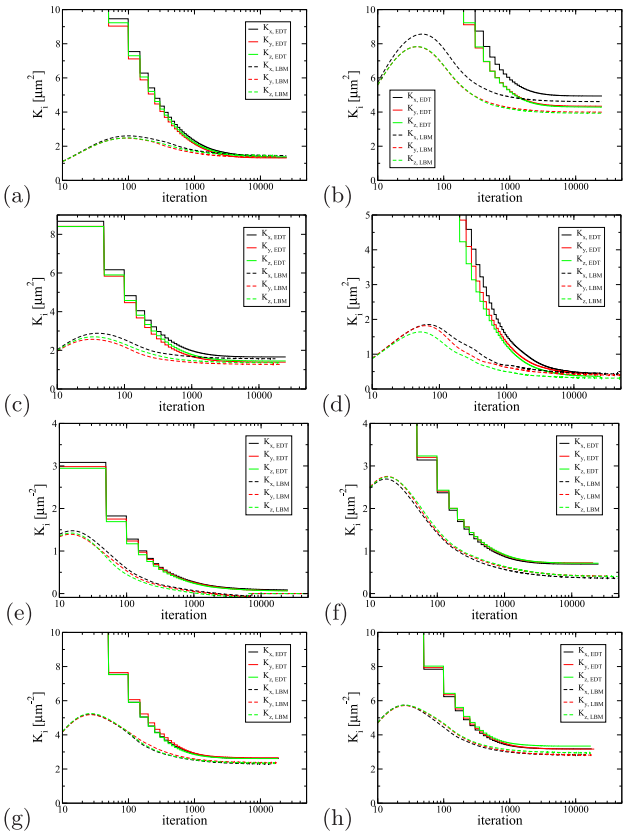

FIG. 9. Comparison of permeability convergence behavior between Laplace approximation and LBM approach for the four outcrop sandstone samples: (a) Berea sandstone, (b) Bentheimer sandstone, (c) Castlegate sandstone, (d) Leopard sandstone, (e–h) Fontainebleau sandstone (480^3, $a = 5.68\,\mu$m; FB08, FB13, FB15, FB22).

The discrepancy between K_{th} and the other estimations is smaller than 7%.

The close packing of spheres arranged in a simple cubic array is of particular interest. Calculations are performed for a solid particle of radius $R/a = 12.5$ located in a cubic unit cell of size $51a$. After discretization, the numerical value of the concentration is equal to 0.458, which is significantly different of the theoretical value equal to $\pi/6$. Figure 1 of Ref. [23] provides k_{ZH} as a function of c; a graphical interpolation yields $k_{\mathrm{ZH}} = 30$. Numerical calculations were performed as before, and we obtain

$$\frac{K_{th}}{a^2} = 2.21, \quad \frac{K_L}{a^2} = 2.31,$$
$$\frac{K_{LBM}}{a^2} = 2.31, \quad \frac{K_{\mathrm{MAC}}}{a^2} = 2.13. \tag{26}$$

The discrepancy between K_{th} and the other estimations is smaller than 5%.

It can be concluded that the Laplace solver provides satisfactory results for cubic arrays of spheres as well.

TABLE III. Comparison of Laplace solver approximation and SRT lattice Boltzmann method for five outcrop sandstones (BE = Berea, BH = Bentheimer, CG = Castlegate, LP = Leopard, FB = Fontainebleau). RAM use (in GB), number of cores (No. cores), and total CPU time t_{CPU} are given for algorithms given in Refs. [3,18,28]; here we report resources and timings for 25 000 iterations of the more recent block-parallel MPI implementation; simulations for FB08 did not converge and were discontinued after 1.5 h and 5000 iterations with negative permeabilities. ϕ includes 50% of the volume fraction of clay regions visible in the segmentation and refers to total porosity. l_{ci}, $i = x,y,z$ refers to the critical diameter (e.g., Ref. [3]) of the resolved pore space in the respective direction using an 18-neighborhood. All permeabilities are given in μm^2; $\alpha = 0.5$.

	BE	BH	CG	LP	FB08	FB13	FB15	FB22
a [μm]	2.334	5.387	3.363	2.151	5.68	5.68	5.68	5.68
Domain	750^3	1200^3	900^3	900^3	480^3	480^3	480^3	480^3
ϕ	0.219	0.245	0.237	0.223	0.083	0.129	0.177	0.210
l_{cx} [μm]	26.0	35.7	22.3	14.3	16.1	25.4	34.1	32.1
l_{cy} [μm]	25.6	35.7	22.3	17.2	19.7	25.4	32.1	32.1
l_{cz} [μm]	26.4	35.7	21.3	12.9	16.1	25.4	32.1	32.1
K'_{Lxx}	1.35	4.94	1.66	0.448	0.086	0.683	2.59	3.14
K'_{Lyy}	1.31	4.34	1.39	0.430	0.068	0.714	2.63	3.13
K'_{Lzz}	1.38	4.30	1.45	0.359	0.064	0.704	2.58	3.30
RAM	83	675	97	97	41	41	41	41
No. cores	64	512	64	64	32	32	32	32
t_{CPU} [h]	288	1280	480	512	2.2	2.2	2.2	3.2
$K'_{xx,\mathrm{LBM}}$	1.45	4.61	1.56	0.427	–	0.356	2.27	2.78
$K'_{yy,\mathrm{LBM}}$	1.36	4.00	1.27	0.393	–	0.407	2.34	2.78
$K'_{zz,\mathrm{LBM}}$	1.46	3.93	1.36	0.307	–	0.400	2.31	2.91
RAM	192	1080	326	327	60	64	63	68
No. cores	80	512	128	128	32	32	32	32
t_{CPU} [h]	818	4352	1132	1680	-	6.6	7.8	8.2

IV. COMPARISON WITH NUMERICAL RESULTS ON REAL SAMPLES

A. Fracture network

The fracture network displayed in Fig. 6 was measured by FIB/SEM with a voxel size of 48.8 nm. The dimensions of the sample are $511 \times 412 \times 206$. It is made spatially periodic along the y axis by replicating its mirror image. Its dimensionless permeability was calculated by LBM, and it was found equal to 9.29×10^{-3}.The solution of the Laplace equation yields a permeability of 8.46×10^{-3} in good agreement with the exact one.

B. Porous media

Consider now the case of Fontainebleau sandstone for the data given in Ref. [18]. Four Fontainebleau sandstone samples of 480^3 voxels each at resolution of $\epsilon = 5.68\,\mu$m are divided into 64 disjoint nonoverlapping blocks of 120^3 voxels each, resulting in 256 data points. We present in Fig. 7 subplots for the comparison of the Laplace solver (k_{EDT}) against LBM (k_{LB}) and experiment as function of porosity, a point-by-point comparison of the Laplace solver against LBM for two discretizations, and the distribution of critical diameter (l_c) at original voxel size ($5.68\,\mu$m) for the considered subsections. The discretisation at $\epsilon = 2.84\,\mu$m is obtained by straight resampling, resulting in 256 blocks of 240^3 voxels. The Laplace solver agrees with experiment for the full range of porosity and performs slightly better at the low-porosity end. The latter is due to discretization effects, which are known to impact LBM solutions when the critical diameter of percolation falls below 4–5 voxels [3]. Figure 7(b) illustrates the critical radius distribution for the case of original image resolution of $\epsilon = 5.68\,\mu$m. Most data exhibit a critical diameter of $\geqslant$4 voxels. Comparing the two solvers at the finer discretization level with $\epsilon = 2.84\,\mu$m shows excellent agreement between the solvers and the tendency for LBM to overpredict at low porosity due to the decreasing critical diameter is removed.

In addition to Fontainebleau sandstone we report results for four outcrop sandstone samples: Berea, Bentheimer, Castlegate, and Leopard sandstone (see Fig. 8). The samples were imaged at the UNSW Tyree helical micro-CT facility and segmented into phases using a converging active contour method [27]. Subdomains for computations are chosen using practical considerations rather than representative volume elements (RVEs), and for the comparison of the two solvers the exact segmentation details or RVE domain choices are not important. The samples cover a range of resolutions and in terms of critical diameter test the higher end of the proposed Laplace solver approach. Comparisons of the two solvers are given in Table III and the convergence behavior depicted in Fig. 9 including for the four 480^3 Fontainebleau sandstone samples. Both solvers give similar results for realistic microstructure based computations even for the case of large critical radius in units of voxels; e.g., for Berea the critical radius $l \geqslant 10$ voxels, yet the relative difference between solvers is below 5%. In all cases considered the relative difference is below 11%, with a typical range of 4%–8% difference and both underprediction by the Laplace approximation (Berea) or overprediction (Bentheimer, Castlegate, Leopard). We further note that for FB08, the low-porosity Fontainebleau sample, no stable solution using the LBM technique was achieved, while for FB13 a still low value for permeability is calculated with LBM. Resource usage is significantly higher for the LBM approach (see Table III)

without using preconditioners in the Laplace solver or making specific optimizations for nonconducting elements. While we report here a speed-up factor of 3–4, significantly better speed-up factors should be achievable by considering preconditioners and implementing sparse implementations applicable in particular for the case of low-porosity samples with insulating matrix.

V. CONCLUDING REMARKS

We presented a robust method to approximately solve for the permeability of a porous medium based on estimating the actual local fluid conductance through a distance map. In particular, we utilize directly the Euclidean distance map resulting in a method which is very easy to implement. The superiority of the method for tomographic images with limited resolution, where the direct application of LBM may fail due to channel width of critical diameter below 4 voxels, is demonstrated. This is a significant development, since for many heterogeneous samples grid refinement comes at a huge cost of not covering larger length scales, e.g., reducing the domain size or covered field of view directly at the imaging stage. The prediction of permeability for low-resolution acquisitions where the pore space stays connected, but below a critical diameter of 4 voxels, can thus be achieved either by applying correlations utilizing critical diameter and effective conductivity ([3]) or by applying the Laplace technique introduced here.

ACKNOWLEDGMENTS

C.H.A. thanks the Australian Research Council for a Future Fellowship (FT120100216) and the ANU/UNSW Digital Core Consortium for support. This research was undertaken with the assistance of resources and services from the National Computational Infrastructure (NCI, Grant m65), which is supported by the Australian Government. P.M.A. thanks the members of the UNSW NMR satellite to the ANU/UNSW Digital Core Consortium for partial support during the stays at UNSW where this work was completed.

[1] P. M. Adler, *Porous Media: Geometry and Transports* (Butterworth-Heinmann, Stoneham, 1992).
[2] M. Sahimi, *Flow and Transport in Porous Media and Fractured Rock* (Wiley-VCH, Weinheim, Germany, 1995).
[3] C. H. Arns, M. A. Knackstedt, and N. S. Martys, Phys. Rev. E **72**, 046304 (2005).
[4] P. A. Lock, X. Jing, R. W. Zimmerman, and E. M. Schlueter, J. Appl. Phys. **92**, 6311 (2002).
[5] A. J. Katz and A. H. Thompson, J. Geophys. Res. **92**, 599 (1987).
[6] F. Bauget, C. H. Arns, M. Saadatfar, M. L. Turner, A. P. Sheppard, R. M. Sok, W. V. Pinczewski, and M. A. Knackstedt, in *19th International Symposium of the Society of Core Analysts* (Toronto, 2005), SCA2005-19.
[7] V. Shabro, C. Torres-Verdin, F. Javadpour, and K. Sepehrnoori, Transp. Porous Media **94**, 775 (2012).
[8] T. Saito and J.-I. Toriwaki, Pattern Recognition **27**, 1551 (1994).
[9] J. Happel and H. Brenner, *Low Reynolds Number Hydrodynamics* (Prentice-Hall, Englewood Cliffs, NJ, 1965).
[10] I. S. Gradshteyn and I. M. Ryzhik, *Tables of Integrals, Series and Products* (Academic Press, New York, 1965).
[11] G. R. McNamara and G. Zanetti, Phys. Rev. Lett. **61**, 2332 (1988).
[12] L.-S. Luo, Phys. Rev. E **62**, 4982 (2000).
[13] Y. H. Qian, D. D'Humieres, and P. Lammelland, Europhys. Lett. **2**, 291 (1986).
[14] C. Pan, L. S. Luo, and C. T. Miller, Comput. Fluids **35**, 898 (2006).
[15] L. Talon, D. Bauer, N. Gland, S. Youssef, and H. A. A. I. Ginzburg, Water Resourc. Res. **48**, 1 (2012).
[16] N. S. Martys, J. G. Hagedorn, D. Goujon, and J. E. Devaney, SPIE **309**, 205 (1999).
[17] B. Ferreol and D. H. Rothman, Transp. Porous Media **20**, 3 (1995).
[18] C. H. Arns, M. A. Knackstedt, W. V. Pinczewski, and N. S. Martys, J. Petr. Sci. Eng. **45**, 41 (2004).
[19] C. Manwart, U. Aaltosalmi, A. Koponen, R. Hilfer, and J. Timonen, Phys. Rev. E **66**, 016702 (2002).
[20] E. L. Wachpress, *Iterative Solutions of Elliptic Systems* (Prentice-Hall, Englewood Cliffs, NJ, 1965).
[21] A. Henriette, C. G. Jacquin, and P. M. Adler, Phys. Chem. Hydrodyn. **11**, 63 (1989).
[22] A. E. Malevich, V. V. Mityushev, and P. M. Adler, Acta Mech. **182**, 151 (2006).
[23] A. A. Zick and G. M. Homsy, J. Fluid Mech. **115**, 13 (1982).
[24] A. S. Sangani and A. Acrivos, Int. J. Multiphase Flow **8**, 343 (1982).
[25] D. Coelho, M. Shapiro, J.-F. Thovert, and P. M. Adler, J. Coll. Interf. Sci. **181**, 169 (1996).
[26] Y. Song, C. A. Davy, T. N. Kim, D. Troadec, G. Hauss, L. Jeannin, and P. M. Adler, Phys. Rev. E **94**, 043316 (2016).
[27] A. P. Sheppard, R. M. Sok, and H. Averdunk, Physica A **339**, 145 (2004).
[28] C. H. Arns, M. A. Knackstedt, W. V. Pinczewski, and W. B. Lindquist, Geophys. Res. Lett. **28**, 3361 (2001).